Fast Spin-Flip Enables Efficient and Stable Organic Electroluminescence from Charge-Transfer States

Lin-Song Cui[1,#], Alexander J. Gillett[1, #], Shou-Feng Zhang[2,3, #], Hao Ye[4], Yuan Liu[5], Xian-Kai Chen[3,*], Ze-Sen Lin[4], Emrys W. Evans[1], William K. Myers[6], Tanya K. Ronson[7], Hajime Nakanotani[4], Sebastian Reineke[5], Jean-Luc Bredas[3], Chihaya Adachi [4,*], Richard H. Friend[1,*]

[1]Cavendish Laboratory, University of Cambridge, JJ Thomson Avenue, Cambridge, CB3 0HE, United Kingdom.

[2]Department of Electronic Engineering, Guangxi University of Science and Technology, Liuzhou 545006, China

[3]School of Chemistry and Biochemistry, Center for Organic Photonics and Electronics, Georgia Institute of Technology, Atlanta, GA, 30332-0400, USA

[4]Center for Organic Photonics and Electronics Research (OPERA), Kyushu University, 744 Motooka, Nishi, Fukuoka 819-0395, Japan.

[5]Dresden Integrated Center for Applied Physics and Photonic Materials (IAPP), Technische Universität Dresden, Dresden, 01069, Germany.

[6]Centre for Advanced Electron Spin Resonance (CAESR), University of Oxford, South Parks Road, Oxford, OX1 3QR, UK.

[7]Department of Chemistry, University of Cambridge, Lensfield Road, Cambridge, CB1EW, United Kingdom.

# These authors contributed equally to this work.

∗ Authors to whom correspondence should be addressed:

E-mail: rhf10@cam.ac.uk (RHF); adachi@cstf.kyushu-u.ac.jp (AC);

chenxiankai@email.arizona.edu (XKC)

A spin-flip from a triplet to a singlet excited state, that is, reverse intersystem crossing (RISC), is an attractive route to harvest triplet excitons for light emission in organic light-emitting diodes (OLEDs). High external quantum efficiencies (EQE) have been obtained via thermally activated delayed fluorescence (TADF) that exploits this RISC mechanism. However, device stability and efficiency roll-off remain challenging issues that originate from the slow RISC rate (k_{RISC}), with the resulting long triplet exciton lifetime leading to severe exciton annihilation processes. Here, we demonstrate that the introduction of multiple donor units that form charge-resonance-type hybrid triplet states leads to a small singlet-triplet energy splitting, large spin-orbit couplings, and a dense manifold of triplet states energetically close to the singlet state. Because of these attributes, k_{RISC} in our novel TADF molecule is as fast as $1.5 \times 10^7 \, \text{s}^{-1}$: a value some two orders of magnitude higher than those in typical TADF emitters. OLEDs based on this molecule serving as an emitter or a sensitizer exhibit long-term stability (the time to reach 90% of the initial brightness of $1000 \, \text{cd} \, \text{m}^{-2}$ is estimated to be about 600 hours), very high efficiency ($\text{EQE}_{max} > 29.3\%$), and a remarkably low efficiency roll-off ($< 2.3\%$ EQE roll-off at $1{,}000 \, \text{cd} \, \text{m}^{-2}$). Our work offers guidelines to design purely organic molecules with a fast k_{RISC}, which will ultimately facilitate OLED applications exploiting the TADF mechanism.

Main

The triplet excited states of organic π-conjugated molecules play an essential role in organic optoelectronic devices, such as organic light-emitting diodes (OLEDs), organic solar cells, and organic semiconductor lasers.[1,2,3,4] Efficiently harvesting triplet excitons is critical in OLEDs, since spin-statistical charge recombination leads to the formation of triplet to singlet excitons in a 3:1 ratio.[5,6,7,8,9,10,11,12] Recent developments have shown that purely organic emitters exploiting thermally activated delayed fluorescence (TADF) in OLEDs can achieve nearly 100% internal quantum efficiencies (IQE).[13,14,15,16,17] However, severe issues still plague TADF-based OLEDs: for example, operational stability and efficiency roll-off remain unsatisfactory, which largely limits their potential for commercialization.[18,19,20,21]

In TADF emitters, a fast reverse intersystem crossing (RISC) process from the triplet to the singlet state is crucial to the efficient utilization of triplet excitons. Early on, RISC was considered to be a process involving simply the lowest triplet (T_1) state and the lowest singlet (S_1) excited state: the degree (α) of mixing of these states can be expressed in the framework of first-order perturbation theory as $\alpha \propto SOC_{S_1-T_1}/\Delta E_{S_1-T_1}$, where $SOC_{S_1-T_1}$ and $\Delta E_{S_1-T_1}$ denote the spin-orbit coupling (SOC) between the S_1 and T_1 states and their energy gap, respectively.[22] This relationship suggests small $\Delta E_{S_1-T_1}$ and large $SOC_{S_1-T_1}$ values are required in order to facilitate efficient RISC. Over the past decade, small $\Delta E_{S_1-T_1}$ (*e.g.*, < 0.1 eV) values have been reported in a broad series of simple donor-acceptor (D-A)-type molecules: in such instances, the spatial separation between the highest occupied and lowest unoccupied molecular orbitals (HOMO and LUMO) leads to very small electron-exchange energy (equal to $\Delta E_{S_1-T_1}/2$ when the main electronic configuration describing both the S_1 and T_1 states simply corresponds to a HOMO-to-LUMO transition).[23,24,25,26,27,28,29,30,31,32,33] In such D-A-type molecules, however, the S_1 and T_1 states often have a dominant charge-transfer (CT) -exciton

character, which results in a vanishingly small SOC (*e.g.*, on the order of < 0.1 cm^{-1}) between the two CT states.[34] The consequence of this negligible SOC is that RISC from a CT-type T_1 to a CT-type S_1 is inefficient even when $\Delta E_{S_1-T_1}$ is small, leading to rate constants (k_{RISC}) in most of the reported TADF emitters lower than 10^6 s^{-1}.[35,36,37,38] The negative outcome of a slow RISC process is long triplet exciton lifetimes, resulting in bimolecular exciton annihilation processes that are responsible for the severe efficiency roll-offs and material degradation occurring in TADF-based OLEDs.[39,40,41,42,43] Thus, designing novel TADF molecules with fast RISC rates is highly desirable to improve OLED stability and efficiency.

Our earlier theoretical investigations on Cz-TRZ (9-(4-(4,6-diphenyl-1,3,5-triazine-2-yl)phenyl)-9H-carbazole) and its derivatives indicated that the T_1-state wavefunctions in these molecules are confined to the carbazole-phenylene-triazine fragment.[44] Importantly, it was predicted that the introduction of additional carbazole donors (which have a high-energy triplet state) would decrease the S_1-state energies but would have little impact on the T_1-state energies and wavefunctions: the consequence is not only a reduced $\Delta E_{S_1-T_1}$ value but also S_1 and T_1 states with different excitation characters.[44] Additionally, we have shown that in D-A-type TADF molecules, the introduction of multiple donor moieties that result in the formation of charge-resonance-type hybrid triplet states leads to the appearance of a dense manifold of triplet states. This opens up additional RISC transition channels from higher-lying triplet (*e.g.*, T_2) states to S_1 (via a second-order spin-vibronic mechanism), which eventually facilitates the spin-flip processes.[45,46]

Based on these earlier findings,[44,45,46] we have designed and synthesized a novel TADF emitter consisting of five carbazole (Cz) donors and one triazine (TRZ) acceptor, *i.e.*, 5Cz-TRZ (9,9',9'',9''',9''''-(6-(4,6-diphenyl-1,3,5-triazine-2-yl)benzene-1,2,3,4,5-pentayl)pentakis(9H-carbazole)), see **Fig. 1a**. For the sake of comparison, we have also investigated three other molecules: mCz-TRZ (9-(4-(4,6-diphenyl-1,3,5-triazin-2-yl)phenyl)-3,6-dimethyl-9H-

carbazole), TmCz-TRZ (9,9′,9″-(5-(4,6-diphenyl-1,3,5-triazine-2-yl)benzene-1,2,3-triyl) tris(3,6-dimethyl-9H-carbazole)), and DACT-II (9-[4-(4,6-diphenyl-1,3,5-triazine-2-yl)phenyl]-N,N,N0,N0-tetraphenyl-9H-carbazole- 3,6-diamine)), see **Fig. 1a**. We demonstrate below that in addition to the appearance of a dense triplet-state manifold, a small $\Delta E_{S_1-T_1}$ and a large spin-orbit coupling are simultaneously achieved in 5Cz-TRZ. As a result, 5Cz-TRZ shows an ultra-fast k_{RISC}, ~ 1.5×10^7 s^{-1}, a value some two orders magnitude faster than those found in the conventional TADF molecules.[16,17,19,21,28] Such a fast RISC process reduces the triplet exciton concentration and the number of bimolecular annihilation events in the emission layer, which in-turn increases the lifetimes of the TADF-based OLEDs more than tenfold and overcomes the efficiency roll-off issue. Furthermore, full-colour hyperfluorescent OLEDs exploiting 5Cz-TRZ as a sensitizer also exhibit very high EQE values of over 24.9%. Our achievement of a fast k_{RISC} (>10^7 s^{-1}) in purely organic molecules opens the door to highly efficient and stable TADF-based OLEDs.

Results and discussion

Computational Results

As shown by the Natural Transition Orbital (NTO) analysis in **Fig. 1b**, the S_1 state of 5Cz-TRZ shows a pronounced CT-excitation character; the hole and electron wavefunctions are localized at the ortho- and meta-carbazole donors and the central (para-carbazole)-phenylene-triazine, respectively, with a small spatial overlap ($O_{h/e}$) of ~ 0.3. In contrast, the T_1 state shows a hybrid character as it consists of local and CT excitations with a large $O_{h/e}$ of ~ 0.7. (see the "**Computational Details**" section for more details on the calculations). The marked difference in the excitation characters of the S_1 and T_1 states results in a significant $SOC_{S_1-T_1}$ value of ~ 0.4 cm^{-1}. Intriguingly, the calculations predict a $\Delta E_{S_1-T_1}$ value as small as ~ 0.02 eV, which is usually obtained in case where S_1 and T_1 both have CT character. The central (para-carbazole)-

phenylene-triazine present in 5Cz-TRZ has a low-energy triplet state at ~ 2.92 eV due to the large electronic coupling between the para-carbazole and phenylene-triazine fragments, see **Fig. 1c**. The additional ortho- and meta-carbazole donors in 5Cz-TRZ possess higher-energy triplet states (~ 3.61 eV), which have little effect on the T_1-state energy (~ 2.95 eV at the T_1-state equilibrium geometry) of the whole 5Cz-TRZ molecule (**Fig. 1c**), a result consistent with our earlier calculations.[44] In contrast, the additional donors largely stabilize the S_1-state energy of 5Cz-TRZ due to electronic delocalization and polarization effects. The consequence is the realization of both a large $SOC_{S_1-T_1}$ and a small $\Delta E_{S_1-T_1}$ value in 5Cz-TRZ. In addition, as demonstrated in our earlier investigations,[46] the Cz donors connected to the phenylene-triazine acceptor leads to a dense manifold of triplet states (with a small energy gap between T_1 and T_2, ~ 0.24 eV), due to the formation of charge-resonance-type hybrid triplet states, see **Fig. 1b**. Another feature is that the $SOC_{S_1-T_2}$ (SOC between the T_2 and S_1 states, ~ 1.3 cm^{-1}) is significantly larger than $SOC_{S_1-T_1}$, a consequence of the differences in the spatial distributions of the T_1 and T_2 hole wavefunctions (**Fig. 1b**). In the framework of Marcus electron-transfer theory, the rate constants from the T_1 and T_2 to S_1 ($k_{T_1 \rightarrow S_1}$ and $k_{T_2 \rightarrow S_1}$) are evaluated to be 4.1 $\times 10^6$ and 1.4×10^9 s^{-1}, respectively. Importantly, the small energy gap between the T_1 and T_2 states opens a spin-flip channel from T_2 to S_1 in addition to the T_1-to-S_1 channel, which implies that the RISC rate in 5Cz-TRZ must be larger than 4.1×10^6 s^{-1}.

It is obvious from the above discussion that our current molecular-design strategy for 5Cz-TRZ is based on two ideas: (i) Whilst the T_1 exciton is confined in the (para-carbazole)-phenylene-triazine segment and has a low triplet energy, the introduction of the additional Cz donors in the ortho- and meta-positions significantly decreases the S_1-state energy, which ultimately reduces the $\Delta E_{S_1-T_1}$ value. Additionally, since we have confined the T_1 state, it now possesses a local-excitation (LE) character, whilst the S_1 state has a CT character; as a result the spin-orbit coupling between the LE-dominated T_1 state and the CT-dominated S_1 state is

strong. (ii) The introduction of the additional Cz donors in the ortho- and meta-positions leads to another positive characteristic, i.e., a dense manifold of triplet states due to the formation of charge-resonance-type hybrid triplet states, which opens up the T_2-to-S_1 RISC channel, in addition to the T_1-to-S_1 channel.

The data for the other three molecules (mCz-TRZ, TmCz-TRZ, and DACT-II) we examined for the sake of comparison are given in **Supplementary Fig. S1** and **Table S1**. In these molecules, the absence of multiple donor groups that could form charge-resonance-type hybrid triplet states results in RISC rates that are 1 to 4 orders of magnitude slower than in 5Cz-TRZ, which significantly hinders their electroluminescent performance and device stability.

Photophysical Properties

The photophysical properties of 5Cz-TRZ were analysed using ultraviolet-visible (UV/Vis) and photoluminescence (PL) spectroscopies. As shown in **Fig. 2a**, the absorption spectrum of 5Cz-TRZ is formed from the combination of the Cz donor and TRZ acceptor absorptions, with an additional weak absorption band between 380 – 420 nm that is attributed to the intramolecular CT transition from the Cz donors to the TRZ acceptor. With increasing solvent polarity, the emission spectrum of 5Cz-TRZ was observed to broaden and red-shift from 470 nm (cyclohexane) to 550 nm (dimethyl formamide), which is consistent with the strong CT character of its first singlet excited state. **Fig. 2b** displays the PL and phosphorescence (Phos) spectrum of 5Cz-TRZ in a frozen toluene matrix at 77 K. As expected, the Phos spectrum of 5Cz-TRZ is well resolved and shows a characteristic vibrational structure, indicating that the T_1 state is not a pure CT state but has LE character as well. In addition, the transient electron spin resonance (TrESR) measurements for 5Cz-TRZ showed relatively broad, polarized spin resonance signals that are indicative of T_1 states formed following spin-orbit-coupling-

mediated intersystem crossing[47] (see **Fig. 2c**, and **Supplementary Table S2** for more detailed discussion of the data). The S_1 and T_1 state energies of 5Cz-TRZ are estimated to be 2.85 and 2.79 eV from the onset of low-temperature PL and the first peak of Phos spectra, respectively, resulting in a 0.06 eV $\Delta E_{S_1-T_1}$ value. These experimental data thus point both to a small $\Delta E_{S_1-T_1}$ and to S_1 and T_1 states with different excitation characters, which is consistent with our theoretical results.

In order to evaluate the delayed fluorescence behaviour, the transient PL characteristics were analysed in degassed solutions at room temperature (**Fig. 2d**). 5Cz-TRZ exhibits clear prompt and delayed fluorescence components. As an example, the delayed exciton lifetime of 5Cz-TRZ is as short as 0.8 μs in dimethyl formamide. The k_{RISC} value was estimated from the PL quantum efficiencies (PLQE) and the exciton lifetime of the prompt and delayed components (a detailed description of the calculations is provided in the **Supplementary Information**). 5Cz-TRZ shows an extremely fast k_{RISC} of $\sim 1.5 \times 10^7$ s^{-1} in toluene, which is some two orders of magnitude higher than those of conventional TADF molecules such as TmCz-TRZ and DACT-II (**Supplementary Fig. S6 and Table S3**). We also investigated the excited-state dynamics of 5Cz-TRZ using pump-probe transient absorption (TA) spectroscopy (**Fig. 2e**). The picosecond TA measurement spectra exhibit broad photoinduced absorption (PIA) signals over the entire spectral region (500 – 1025 nm); the signals undergo rapid spectral shifts within the first 10 ps, which can be assigned to structural and solvent reorganization processes[48] (more detailed discussions of the dynamical processes can be found in the **Supplementary Information**). Nanosecond TA was also performed to investigate the timescales of ISC/RISC and to characterize triplet excited-state features. As illustrated by **Figs. 2f and g**, 5Cz-TRZ undergoes ISC from the ^{1}CT state to the triplet manifold with a time constant of 4.5 ns, which is shorter than those of TmCz-TRZ and DACT-II (**Supplementary Figs. S7 and 8**). The near degenerate singlet and triplet states, together with the large spin-

orbit couplings, are responsible for the rapid ISC times observed in 5Cz-TRZ. Time-resolved temperature-dependent PL decay data for 15wt%-doped films of 5Cz-TRZ in *m*CBP were also collected to further investigate their excited-state decay kinetics (**Fig. 2h**). The RISC rates are observed to increase with increasing temperature from 200 to 300 K (**Fig. 2i**) and reach 1.37×10^7 s^{-1} at 300 K. The $\Delta E_{S_1 - T_1}$ value estimated is 0.03 eV from the Arrhenius plots of the k_{RISC} values in 5Cz-TRZ (**Supplementary Fig. S5**).

Device characterization

Given the promising photophysical properties of 5Cz-TRZ, which include fast k_{RISC} and high PLQE, its EL performance was evaluated. The optimized device configuration shown in **Fig. 3** has the following architecture: ITO/HAT-CN (10 nm)/α-NPD (30 nm)/Tris-PCz (10 nm)/*m*CBP (6 nm)/15 wt% TADF emitter: *m*CBP (20 nm)/CF3-TRZ (10 nm)/30 wt% Liq: BPPB (45 nm)/Liq (2 nm)/Al (120 nm), where HAT-CN, α-NPD, Tris-PCz, *m*CBP, CF3-TRZ and BPPB are 1,4,5,8,9,11-hexaazatriphenylene hexacarbonitrile, N,N′-diphenyl-N,N′-bis(1-naphthyl)−1,10-biphenyl-4,4′-diamine, 9,9′,9″-triphenyl-9H,9′H,9″H−3,3′:6′3″-tercarbazole, 3,3-di(9H-carbazol-9-yl)biphenyl, 6,6'-((perfluoropropane-2,2-diyl)bis(4,1-phenylene))bis(2,4-diphenyl-1,3,5-triazine) and 1,3-bis(9-phenyl-1,10-phenanthrolin-2-yl)benzene, respectively; 15wt% of 5Cz-TRZ doped in *m*CBP (device A) served as the emitting layer (EML). For comparison, the control devices (devices B and C) were fabricated with the TmCz-TRZ and DACT-II emitters. The materials used and the device structures are given in **Supplementary Fig. S10.**

Devices A and B show sky-blue emission with EL peaks at 486 and 496 nm, respectively, whereas device C exhibits pure green emission with the emission peak at 530 nm (**Fig. 4b**). As illustrated in **Fig. 4a** and **Supplementary Fig. S11**, high and stable efficiencies are achieved with device A. The maximum EQE of device A is 29.3%, a value much higher

9

than those of device B (19.7%) and device C (24.3%). It is especially noteworthy that device A, which has 5Cz-TRZ as dopant, exhibits an extremely low efficiency roll-off. For example, the efficiency remains at 28.6% at 1000 cd m^{-2} and still as high as 27.0% at 5000 cd m^{-2}, corresponding to a 2.3% and 7.8% decrease in EQE at these brightness points. In contrast, devices B and C display severe efficiency roll-off with much lower EQEs of only 8.6% and 16.2% at 5000 cd m^{-2}, which corresponds to 56.3% and 33.3% decreases in EQE, respectively.

The transient EL decay characteristics at different luminance levels were used to further confirm the low efficiency roll-off behaviour of the 5Cz-TRZ-based device (see **Fig. 4c**),with very little reduction in the excition lifetime observed at high luminance levels. With this impressive behaviour confirmed, we then analysed the operational stability of the devices (**Fig. 4d**), showing that the T_{90} (time to reach 90% of initial luminance) values of devices A, B, and C are 35.4, 3.2, and 5.1 h for an initial brightness (L_0) of 5000 cd m^{-2}. Device A thus exhibited by far the longest operational stability, with device lifetime over ten times longer than that of device B. The T_{90} of device A is predicted to be 592.2 h at 1000 cd m^{-2} according to the formula $LT(L_1) = LT(L_0) \times (L_0/L_1)^n$, where L_1 is the initial luminance of 1000 cd m^{-2} (n=1.75, which is obtained by fitting T_{90} versus L_0 in **Supplementary Fig. S14**).[49] To the best of our knowledge, this result represents the longest device lifetime reported for TADF-based OLEDs (**Supplementary Table S5**).

Hole-only and electron-only devices based on the structures of devices A, B, and C were also fabricated to characterize the carrier-transport properties. All devices exhibited similar properties (**Supplementary Fig. S15**), which implies that charge-carrier transport is not the major factor determining the differences in efficiency roll-off and operational stability. Thus, the reduced efficiency roll-off and improved operational stability of device A is primarily determined by the fast k_{RISC} that limits the amount of bimolecular exciton annihilation processes taking place in the devices.

To better understand the factors behind the high EQE of device A, we investigated the emitting-dipole orientations in these devices using variable-angle PL measurements. As shown in **Supplementary Fig. S16**, the orientation factor (θ) of 5Cz-TRZ is estimated to be 0.17 (we recall that $\theta = 0$ for completely horizontal alignment and 0.33 for isotropic distribution).[50] Using this value, the optical simulation results indicate that device A can achieve a maximum EQE of 30.9%, which is consistent with our experimental data.

The fast k_{RISC} of 5Cz-TRZ inspired us to further investigate the performance of hyperfluorescent OLEDs exploiting 5Cz-TRZ as sensitizer (**Supplementary Fig. S17**). 2,5,8,11-tetra-tert-butylperylene (TBPe), 5,12-Dibutyl-1,3,8,10-tetramethylquinacridone (TMDQA), 2,8-di-tert-butyl-5,11-bis(4-tert-butylphenyl)-6,12-diphenyltetracene (TBRb) and 4-(Dicyanomethylene)-2-tert-butyl-6-(1,1,7,7-tetramethyljulolidin-4-yl-vinyl)-4H-pyran (DCJTB) were selected as sky-blue, green, yellow, and red fluorescent emitter dopants, respectively. Taking the same device structure as for the TADF-emitter-based OLEDs, the hyperfluorescent OLEDs based on 5Cz-TRZ as sensitizer show EQEs as high as 24.0% (device D; sky bule), 22.3% (device E; green), 24.9% (device F; yellow) and 23.5% (device G; red). The slightly lower EQEs and larger efficiency roll-offs vs. the 5Cz-TRZ-emitter-based device are likely due to hole trapping by the fluorescent molecules, as the HOMO levels of the fluorescent materials are shallower compared to that of 5Cz-TRZ. However, the operational lifetimes of the OLEDs based on 5Cz-TRZ as the sensitizer were longer than that of the OLED with 5Cz-TRZ as the emitter dopant (see **Fig. 4d**). We do note that the EL spectrum of device D is somewhat different form its PL spectrum in the co-deposited film (**Supplementary Fig. S18**), which is most likely induced by the microcavity effect of the device rather than an incomplete energy transfer.[21]

Finally, we constructed a white OLED (device H) by employing 5Cz-TRZ as the sky-blue emitter, complemented by TBRb and DCJTB as yellow and red emitters, respectively. A

high EQE of 21.8 % was achieved with Commission Internationale de I'Eclairage (CIE) coordinates of (0.43, 0.45) and colour rendering index (CRI) of 81 (**Fig. 4b**).

Conclusion

In summary, we have designed a sky-blue metal-free organic emitter (5Cz-TRZ) with a RISC rate as fast as 1.5×10^7 s^{-1}, some two orders of magnitude higher than the typical values for TADF emitters. The introduction of multiple carbazole donors in 5Cz-TRZ that form charge-resonance-type hybrid triplet states leads simultaneously to a small single-triplet energy splitting, large spin-orbit coupling, and dense triplet-state manifold, which all contribute to the fast RISC. In combination with a near 100% PLQE and a strong horizontal dipole orientation in the doped film, state-of-the-art OLED devices exploiting 5Cz-TRZ as emitter show a maximum EQE of 29.3%, a low efficiency roll-off at high luminance (*e.g.* a mere 2.3% roll-off of the EQE at 1,000 cd m^{-2}), and an estimated T_{90} value of ~ 600 h for an initial brightness of 1000 cd m^{-2}. Importantly, we note that this lifetime is tenfold longer than that of the reference device based on the TmCz-TRZ emitter, which has a slower k_{RISC}. Additionally, full-colour hyperfluorescent OLEDs exploiting 5Cz-TRZ as a sensitizer reach high EQE values of over 22.0%. Thus, we consider that our novel design strategy represents an important step towards achieving a fast k_{RISC} in TADF molecules, paving the way to efficient and stable TADF and hyperfluorescent OLEDs.

Methods

Synthesis and characterization

The general procedure for the synthesis of the TADF molecules and the characterization of their chemical properties are reported in the Supplementary Information.

Computational details

The initial ground-state geometries of the molecules were optimized with the long-range corrected functional ωB97XD (with the default range-separation parameter ω of 0.2 bohr^{-1}) and the 6-31G(d,p) basis set.[51] Then, following our earlier works,[44,52] an iterative "gap-tuning" procedure was applied to obtain the optimal ω values for these geometries. The Tamm-Dancoff approximation (TDA) was employed in the framework of time-dependent density functional theory (TD-DFT) to study the excited-state properties; all the excited-state properties were examined at the TDA tuned-ωB97XD/6-31G(d,p) level combined with the polarizable continuum model (PCM; implicit solvent: toluene). Natural transition orbital analyses were also performed to examine the nature of the excited states; the spatial overlaps between the density distributions of the hole and electron wavefunctions in the excited states were estimated with the Multiwfn code.[53] All quantum-chemical calculations were performed with the Gaussian 16 program.[54] In addition, the spin-orbit couplings were estimated by employing the Breit-Pauli spin-orbit Hamiltonian with an effective charge approximation, as implemented in the PySOC code.[55]

Absorption, steady-state PL spectra and PLQE measurements

UV-vis and PL spectra were recorded on a Perkin-Elmer Lambda 950 KPA spectrophotometer and JobinYvon FluoroMax-3 fluorospectrophotometer, respectively. Phos spectra were recorded on a JASCO FP-6500 fluorescence spectrophotometer at 77 K. Absolute PL quantum yields were measured on a Quantaurus-QY measurement system (C11347-11, Hamamatsu Photonics) under nitrogen flow and all samples were excited at 360 nm.

Eectron paramagnetic resonance (EPR) measurements

Transient CW EPR measurements (trEPR) were performed in the Centre for Advanced ESR (CAESR) in the Department of Chemistry of the University of Oxford, using both Bruker BioSpin EleXSys I E680 and EleXSys II E580 spectrometers at X-band, ca. 9.75 GHz. Details of the optical simulations are given in the **Supplementary Information**.

Time-resolved spectroscopic measurements

All the solutions were deoxygenated with dry nitrogen gas to eliminate the deactivation of triplets by oxygen. The transient PL decay characteristics of solution samples were recorded using a Quantaurus-Tau fluorescence lifetime measurement system (C11367-03, Hamamatsu Photonics). Time-resolved PL of the film samples were measured using an Andor electrically gated intensified charge-coupled device and laser excitation at 350 nm. For low-temperature measurements, an Oxford Instruments continuous flow cryostat was used with liquid helium as the coolant. Experimental details for the transient PL and absorption measurements are given in **Supplementary Information**.

Transient absorption (TA) measurements

Sample photoexcitation in the nanosecond transient absorption experiments was achieved by the third harmonic (355 nm) of an electronically triggered Q-switched Nd:YVO$_4$ laser (~1 ns pulse length, Advanced Optical Technologies Ltd AOT-YVO-25QSPX). For the picosecond transient absorption, ~100 fs excitation pulses at 400 nm, generated from the second harmonic of the 800 nm fundamental of the Ti:sapphire laser (Spectra Physics Solstice Ace), was used. For both temporal regions, the probe was generated by home-built broadband visible (500 – 770 nm) and NIR (830 – 1025 nm) non-collinear optical parametric amplifiers (NOPAs), pumped using the frequency-doubled output (400 nm) of the Ti:sapphire laser. The delay between the pump and probe pulses was varied using a Stanford DG645 delay generator for the nanosecond measurements, while a mechanical delay stage (Thorlabs DDS300-E/M) was used to delay the probe with respect to the pump for the picosecond measurements. The transmitted probe pulses were collected with a silicon dual-line array detector (Hamamatsu S8381-1024Q) which was driven and read out by a custom-built board from Stresing Entwicklungsbüro.

Angle-dependent PL measurements

The angle-dependent PL measurement was measured by a spectrometer (Ocean Optics USB 4000) together with a 405 nm continuous wave laser as the excitation source, a half cylindrical lens, a motorized rotation stage, and a polarizer to select p-polarized light. Details of the optical simulations are given in the **Supplementary Information**.

Device fabrication and measurements

OLEDs were fabricated through vacuum deposition of the materials at *ca.* 6.0×10^{-8} Torr onto ITO-coated glass substrates with a sheet resistance of ca. 15 $\Omega/\square$. The ITO surface was sequentially cleaned ultrasonically with acetone, ethanol, and deionized water, dried in an oven, and then exposed to UV/ozone for about 30 min. Organic layers were deposited at a rate of 2–3 Å/s; Liq was subsequently deposited at 0.2 Å/s and then capped with Al (ca. 3 Å/s). The devices were exposed once to nitrogen gas after the formation of the organic layers because a metal mask was included to define the cathode area. For all the OLEDs, the emitting area determined by the overlap of the two electrodes was 4.5 mm^2. Current density-voltage-luminescence (*J-V-L*) characteristics were measured using a Keithley 2400 sourcemeter, Keithley 2000 multimeter and a calibrated silicon photodiode. Time-resolved EL of the samples was recorded by the same ICCD spectrometer used in the time-resolved PL measurements.

Author Contributions

L.S.C. designed the molecules and carried out device fabrication and measurements. A.J.G. conducted the transient absorption experiments. S.-F.Z. performed the theoretical calculations under the supervision of X.-K.C.. Y.L. performed the molecular orientation and optical simulations under the supervision of S. R.. H.Y. and Z.S.L carried out steady-state and time-resolved photophysical properties under the supervision of C.A.. E.W.E. and W.K.M conducted the transient electron spin resonance measurements and analysed the results. T.K.R. performed single crystal X-ray diffraction and analysed the results. H.N. participated in the discussion of the photophysical mechanism. L.S.C., A.J.G., X.-K.C., J.-L.B. and R.H.F. analysed the data and wrote the manuscript. All authors discussed the progress of research and reviewed the manuscript.

Data availability

The data that support the plots within this paper and other findings of this study are available from the corresponding author upon reasonable request.

Competing interests

The authors declare no competing interests.

References

1. Baldo, M. A. et al. Highly efficient phosphorescent emission from organic electroluminescent devices. *Nature* **395,** 151–154 (1998).

2. Einzinger, M. et al. Sensitization of silicon by singlet exciton fission in tetracene. *Nature* **571,** 90–94 (2019).

3. Samuel, I. D. W. & Turnbull, G. A. Organic Semiconductor Lasers. *Chem. Rev.* **107,** 1272–1295 (2007).

4. Kohler, A. & Bassler, H. Triplet states in organic semiconductors. *Mater. Sci. Eng. R* **66,** 71–109 (2009).

5. Adachi, C., Baldo, M. A., Thompson, M. E. & Forrest, S. R. Nearly 100% internal phosphorescence efficiency in an organic light emitting device. *J. Appl. Phys.* **90,** 5048–5051 (2001).

6. Ma, Y., Zhang, H., Shen, J. & Che, C. Electroluminescence from triplet metal-ligand charge-transfer excited state of transition metal complexes. *Synth. Met*. **94,** 245–248, (1998).

7. Köhler, A. & Beljonne, D. The singlet-triplet exchange energy in conjugated polymers. *Adv. Funct. Mater.* **14,** 11–18 (2004).

8. Kondakov, D. Y. Characterization of triplet-triplet annihilation in organic light-emitting diodes based on anthracene derivatives. *J. Appl. Phys.* **102,** 114504 (2007).

9. Ly, K. T. et al. Near-infrared organic light-emitting diodes with very high external quantum efficiency and radiance. *Nat. Photon.* **11,** 63–68 (2017).

10. Li, L. K. et al. Strategies towards rational design of gold(iii) complexes for high-performance organic light-emitting devices. *Nat. Photon.* **13,** 185–191 (2019).

11. Hamze, R. et al. Eliminating nonradiative decay in Cu(I) emitters: >99% quantum efficiency and microsecond lifetime. *Science* **363,** 601–606 (2019).

12. Ai, X. et al. Efficient radical-based light-emitting diodes with doublet emission. *Nature* **563,** 536–540 (2018).

13. Uoyama, H., Goushi, K., Shizu, K., Nomura, H. & Adachi, C. Highly efficient organic light-emitting diodes from delayed fluorescence. *Nature* **492,** 234–238 (2012).

14. Zhang, Q. et al. Efficient blue organic light-emitting diodes employing thermally activated delayed fluorescence. *Nat. Photon.* **8,** 326–332 (2014).

15. Liu, Y., Li, C., Ren, Z., Yan, S. & Bryce, M. R. All-organic thermally activated delayed fluorescence materials for organic light-emitting diodes. *Nat. Rev. Mater.* **3,** 18020 (2018).

16. Wong, M. Y. & Zysman-Colman, E. Purely organic thermally activated delayed fluorescence materials for organic light-emitting diodes. *Adv. Mater.* **29,** 1605444 (2017).

17. dos Santos, P. L. et al. Triazatruxene: A Rigid Central Donor Unit for a D-A$_3$ Thermally Activated Delayed Fluorescence Material Exhibiting Sub-Microsecond Reverse Intersystem Crossing and Unity Quantum Yield via Multiple Singlet-Triplet State Pairs. *Adv. Sci.* **5,** 1700989 (2018).

18. Cui, L.-S. et al. Controlling synergistic oxidation processes for efficient and stable blue thermally activated delayed fluorescence devices. *Adv. Mater.* **28,** 7620–7625 (2016).

19. Noda, H., Nakanotani, H. & Adachi, C. Excited state engineering for efficient reverse intersystem crossing. *Sci. Adv.* **4,** eaao6910 (2018).

20. Cui, L.-S. et al. Long-lived efficient delayed fluorescence organic light-emitting diodes using n-type hosts. *Nat. Commun.* **8,** 2250 (2017).

21. Chan, C.-Y. et al. Efficient and stable sky-blue delayed fluorescence organic light-emitting diodes with CIEy below 0.4. *Nat. Commun.* **9,** 5036 (2018).

22. Turro, N. J., Ramamurthy, V. & Scaiano, J. C. in Principle of Molecular Photochemistry: *An Introduction* Ch. **3,** 113–118 (University Science Books, 2009).

23. Gómez-Bombarelli, R. et al. Design of efficient molecular organic light-emitting diodes by a high-throughput virtual screening and experimental approach. *Nat. Mater.* **15,** 1120–1127 (2016).

24. Kondo1, Y. et al. Narrowband deep-blue organic light-emitting diode featuring an organoboron-based emitter. *Nat. Photon.* **13,** 678–682 (2019).

25. Kotadiya, N., Blom, P. W. M. & Wetzelaer, G.-J. A. H. Efficient and stable single-layer organic light-emitting diodes based on thermally activated delayed fluorescence. *Nat. Photon.* **13,** 765–769 (2019).

26. Ahn, D. H. et al. Highly efficient blue thermally activated delayed fluorescence emitters based on symmetrical and rigid oxygen-bridged boron acceptors. *Nat. Photon.* **13,** 540–546 (2019)

27. Wu, T.-L. et al. Diboron compound-based organic light-emitting diodes with high efficiency and reduced efficiency roll-off. *Nat. Photon.* **12,** 235–240 (2018).

28. Lee, D. R. et al. Design strategy for 25% external quantum efficiency in green and blue thermally activated delayed fluorescent devices. *Adv. Mater.* **27,** 5861–5867 (2015).

29. Wu, K. et al. De novo design of excited-state intramolecular proton transfer emitters via a thermally activated delayed fluorescence channel. *J. Am. Chem. Soc.* **140,** 8877– 8886, (2018).

30. Pershin, A. et al. Highly emissive excitons with reduced exchange energy in thermally activated delayed fluorescent molecules. *Nat. Commun.* **10,** 597 (2019).

31. Sharma, N. et al. Turn on of sky-blue thermally activated delayed fluorescence and circularly polarized luminescence (CPL) via increased torsion by a bulky carbazolophane donor. *Chem. Sci.* **10,** 6689–6696 (2019).

32. Lin, T.-A. et al. Sky-blue organic light emitting diode with 37% external quantum efficiency using thermally activated delayed fluorescence from spiroacridine-triazine hybrid. *Adv. Mater.* **28,** 6976–6983 (2016).

33. Zhang, Y. et al. Multi-resonance induced thermally activated delayed fluorophores for narrowband green OLEDs. *Angew. Chem. Int. Ed.* **131**, 1–7 (2019).

34. El-Sayed, M. A. The radiationless processes involving change of multiplicity in the diazenes. *J. Chem. Phys.* **36,** 573–574 (1962).

35. Olivier, Y. et al. Nature of the singlet and triplet excitations mediating thermally activated delayed fluorescence. *Phys. Rev. Mater.* **1**, 75602 (2017).

36. Marian, C. M. Spin–orbit coupling and intersystem crossing in molecules. *WIREs Comput. Mol. Sci.* **2,** 187– 203, (2012).

37. Etherington, M. K., Gibson, J., Higginbotham, H. F., Penfold, T. J. & Monkman, A. P. Revealing the spin-vibronic coupling mechanism of thermally activated delayed fluorescence. *Nat. Commun.* **7,** 13680 (2016).

38. Penfold, T. J., Gindensperger, E., Daniel, C. & Marian, C. M. Spin-vibronic mechanism for intersystem crossing. *Chem. Rev.* **118,** 6975–7025 (2018).

39. Murawski, C., Leo, K. & Gather, M. C. Efficiency roll-off in organic light-emitting diodes. *Adv. Mater.* **25,** 6801–6827 (2013).

40. Einzinger, M. et al. Shorter exciton lifetimes via an external heavy-atom effect: alleviating the effects of bimolecular processes in organic light-emitting diodes. *Adv. Mater.* **29,** 1701987 (2017).

41. Reineke, S., Schwartz, G., Walzer, K. & Leo, K. Reduced efficiency roll-off in phosphorescent organic light emitting diodes by suppression of triplet-triplet annihilation. *Appl. Phys. Lett.* **91,** 123508 (2007).

42. Lee, J. et al. Hot excited state management for long-lived blue phosphorescent organic light-emitting diodes. *Nat. Commun.* **8,** 1–9 (2017).

43. Munkhbat, B., Wersäll, M., Baranov, D. G., Antosiewicz, T. J. & Shegai, T. Suppression of photo-oxidation of organic chromophores by strong coupling to plasmonic nanoantennas. *Sci. Adv.* **4,** eaas9552 (2018).

44. Chen, X.-K. et al. A new design strategy for efficient thermally activated delayed fluorescence organic emitters: from twisted to planar structures. *Adv. Mater.* **29,** 1702767 (2017).

45. Chen, X. K., Zhang, S. F., Fan, J. X. & Ren, A. M. Nature of highly efficient thermally activated delayed fluorescence in organic light-emitting diode emitters: nonadiabatic effect between excited states. *J. Phys. Chem. C* **119**, 9728–9733 (2015).

46. Noda, H., Chen, X. K. et al. Critical role of intermediate electronic states for spin-flip processes in charge-transfer-type organic molecules with multiple donors and acceptors. *Nat. Mater.* **18,** 1084–1090 (2019).

47. Evans, E. W. et al. Vibrationally assisted intersystem crossing in benchmark thermally activated delayed fluorescence molecules. *J. Phys. Chem. Lett.* **9**, 4053–4058 (2018).

48. Kuang, Z. R. et al. Conformational Relaxation and thermally activated delayed fluorescence in anthraquinone-based intramolecular charge-transfer compound. *J. Phys. Chem. C* **122**, 3727– 3737, (2018).

49. Zhu, Z.-Q., Klimes, K., Holloway, S. & Li, J. Efficient cyclometalated platinum(II) complex with superior operational stability. *Adv. Mater.* **29,** 1605002 (2017).

50. Yokoyama, D. Molecular orientation in small-molecule organic light-emitting diodes. *J. Mater. Chem.* **21,** 19187–19202 (2011).

51. Chen, X.-K., Kim, D. & Bredas, J.-L. Thermally activated delayed fluorescence (TADF) path toward efficient electroluminescence in purely organic materials: molecular level insight. *Acc. Chem. Res.* **51**, 2215−2224 (2018).

52. Chen, X.-K. et al. Intramolecular Noncovalent Interactions Facilitate Thermally Activated Delayed Fluorescence (TADF). *J. Phys. Chem. Lett.* **10,** 3260−3268 (2019).

53. Lu T. & Chen F. Multiwfn: A multifunctional wavefunction analyser. *J. Comput. Chem.* **33**, 580–592 (2012).

54. Frisch, M. J. et al. Gaussian, Inc., Wallingford CT, 2016.

55. Gao, X. et al. Evaluation of Spin-Orbit Couplings with Linear-Response Time-Dependent Density Functional Methods. *J. Chem. Theory Comput*. **13**, 515−524 (2017).
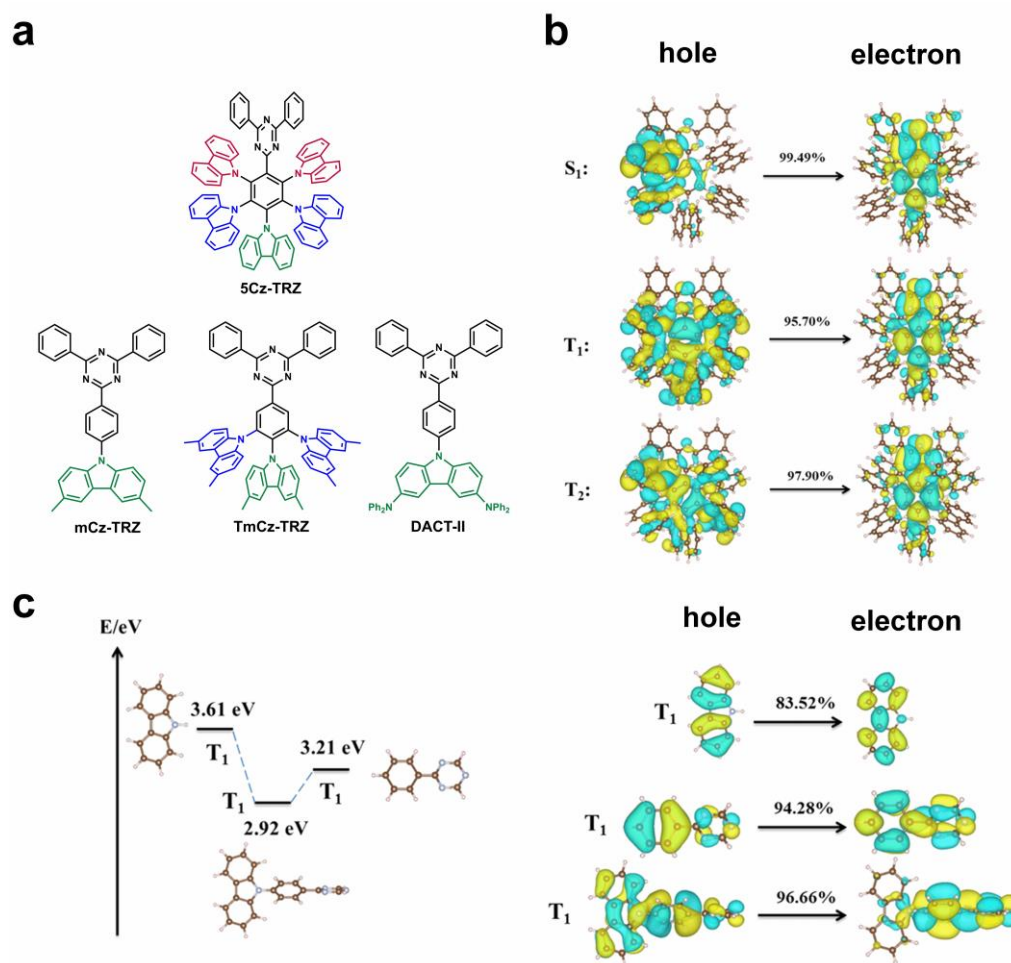
Fig. 1 | Chemical structures and results of quantum-chemical calculations for 5Cz-TRZ, mCz-TRZ, TmCz-TRZ, and DACT-II. (a) Chemical structures of 5Cz-TRZ, mCz-TRZ, TmCz-TRZ, and DACT-II. (b) Natural Transition Orbitals describing the excitation characters of the S_1, T_1, and T_2 states in 5Cz-TRZ; the weights of the hole–electron contributions to the excitations are included. (c) Left: Correlation diagram for the triplet states of the carbazole, phenylene–triazine, and carbazole–phenylene–triazine fragments, based on the T_1 equilibrium geometry of 5Cz-TRZ. Right: Natural Transition Orbitals for the T_1 states in the three fragments.
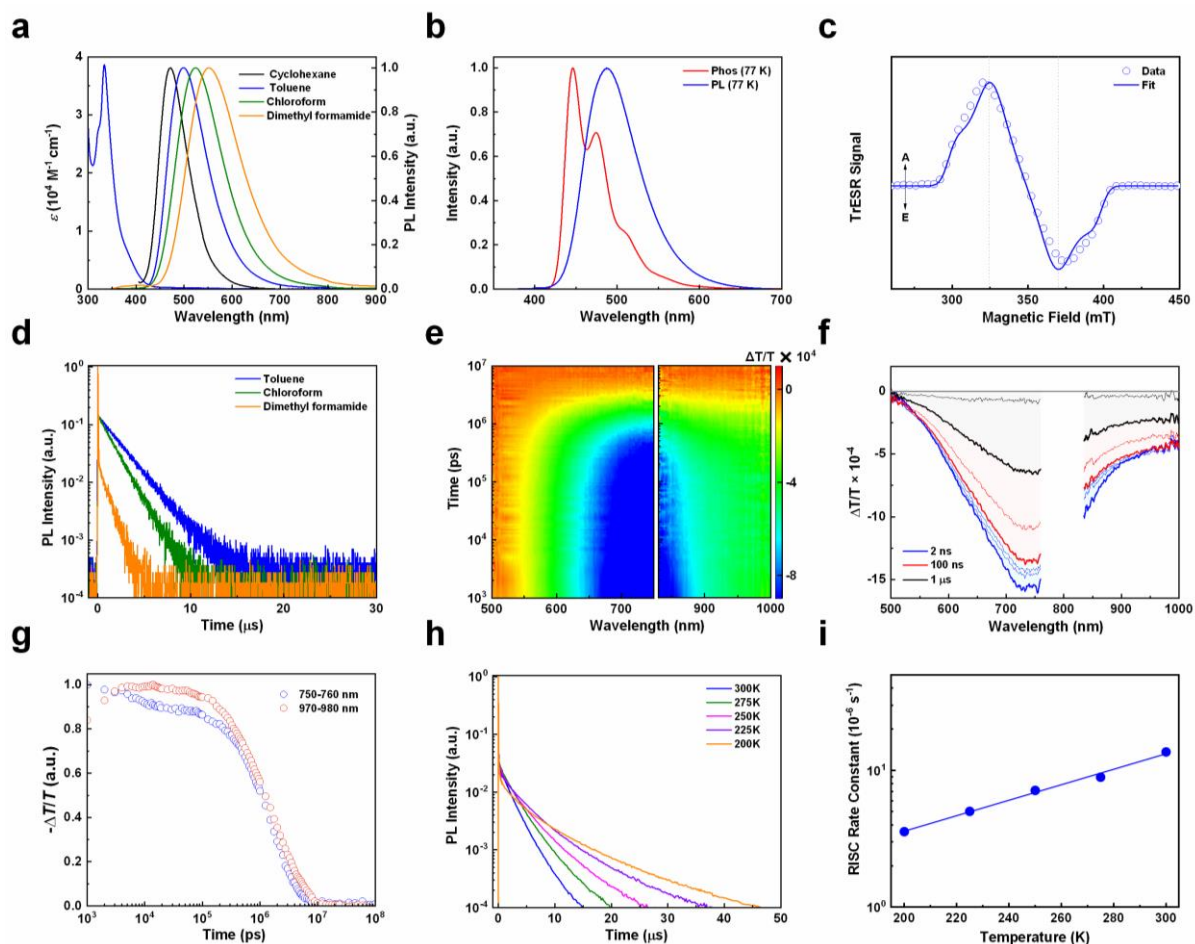
Fig. 2 | Photophysical characterization of 5Cz-TRZ. a, Absorption and PL spectra (300 K) of 5Cz-TRZ in dilute solution (toluene solvent). **b,** Phosphorescent (Phos) and PL spectra of 5Cz-TRZ in toluene glass at 77 K. **c**, TrESR spectra (80 K) of 5Cz-TRZ in dilute toluene solutions. **d,** Transient PL spectra (300 K) of 5Cz-TRZ in oxygen-free dilute solution with different polarity. **e,** Transient absorption contour maps (300 K) of 5Cz-TRZ on nanosecond timescales in oxygen-free toluene. Excitation wavelength: 355 nm, fluence: 5.49 μJ/cm². **f,** Transient absorption spectra (300 K) of 5Cz-TRZ on nanosecond timescales in oxygen-free toluene. **g,** Decay kinetics of the transient absorption taken at 750-760 nm and 970-980 nm. **h,** Temperature-dependent transient PL (200-300 K) decay curves of the 5Cz-TRZ doped film. **i,** Temperature-dependent reverse intersystem crossing (RISC) rate constants of the 5Cz-TRZ doped film.
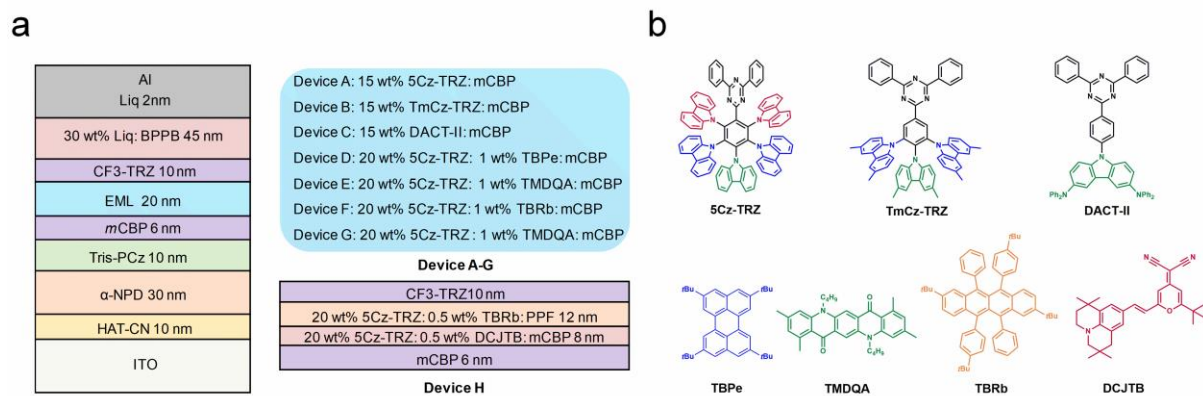
Fig. 3 | Device structures and materials. a, Architectures of the TADF and hyperfluorescent OLEDs. **b,** Chemical structures of the TADF and fluorescent emitters.
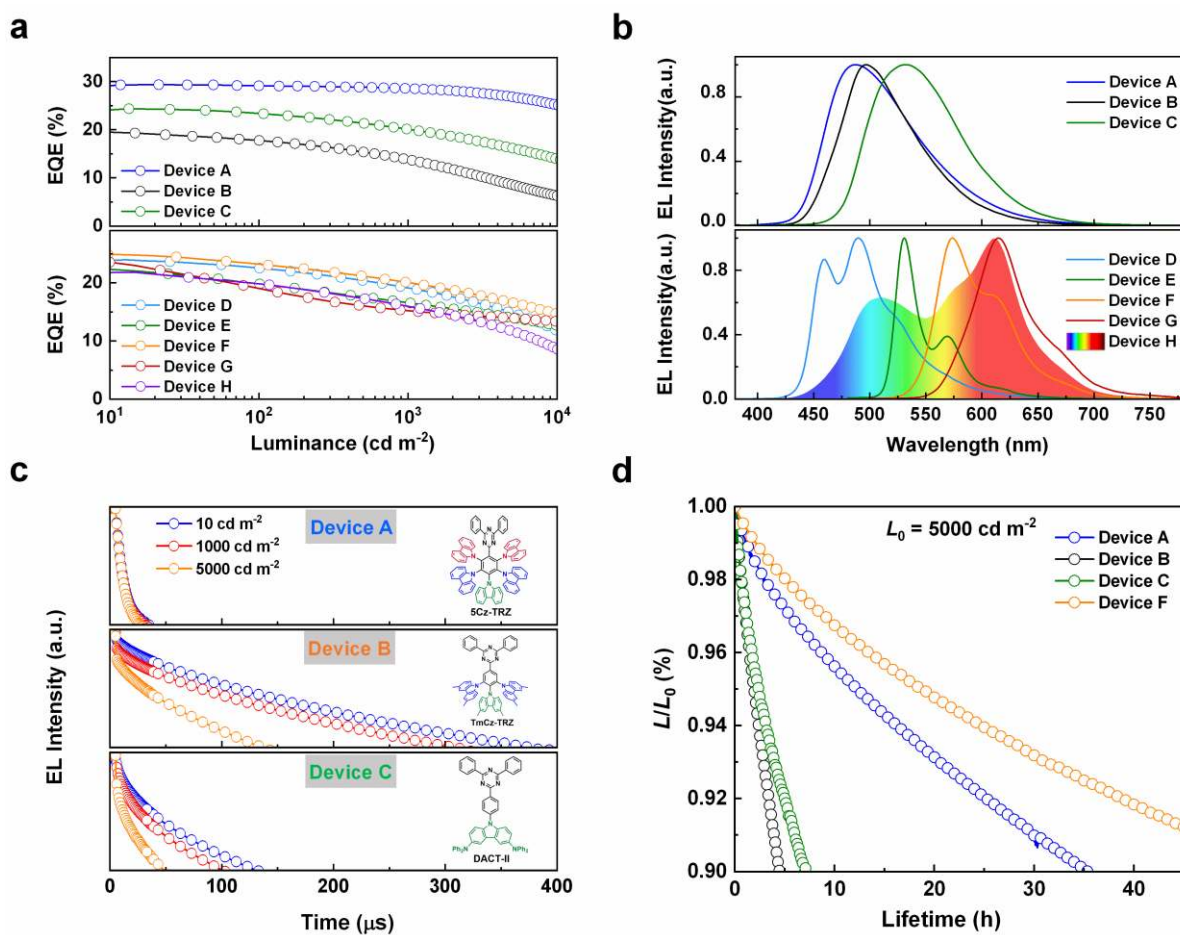
Fig. 4 | Device performance of OLEDs. a, EQE versus luminance characteristics. **b,** Normalized EL spectra. **c,** Transient EL decay characteristics of device A, B, C at 10, 1000, 5000 cd m^{-2}. **d,** Operational lifetimes of the TADF and hyperfluorescent OLEDs.